

Article

Effect of Mo on the Mechanical and Corrosion Behaviors in Non-Equal Molar AlCrFeMnNi BCC High-Entropy Alloys

Wei-Chen Hsu¹, Wei-Pin Kao¹, Jien-Wei Yeh^{1,2} and Che-Wei Tsai^{1,2,*} 

¹ Department of Materials Science and Engineering, National Tsing Hua University, Hsinchu 30013, Taiwan; suprecrazy123123123@gmail.com (W.-C.H.); benkao20411295@gmail.com (W.-P.K.); jwyeh@mx.nthu.edu.tw (J.-W.Y.)

² High Entropy Materials Center, National Tsing Hua University, Hsinchu 30013, Taiwan

* Correspondence: chewei@mx.nthu.edu.tw

Abstract: Co-free body-centered cubic (bcc) high-entropy alloys (HEAs) are prepared, and the elevated mechanical property and corrosion property of the $Al_{0.4}CrFe_{1.5}MnNi_{0.5}Mo_x$ ($x = 0$ and 0.1) alloys are studied. The Vickers hardness (HV) of the as-homogenized state is between HV 350 and HV 400. Both alloys are provided with nano-scale NiAl-rich B2 precipitates which contribute to the strength at high-temperature. In addition, adding Mo in the present alloy strengthens by σ phase. $Al_{0.4}CrFe_{1.5}MnNi_{0.5}Mo_{0.1}$ exhibited outstanding tensile properties, with a yield strength of 413 MPa and ultimate tensile strength of 430 MPa in the elevated tensile test at 600 °C, which is better than that of $Al_{0.4}CrFe_{1.5}MnNi_{0.5}$ alloy. Through potentiodynamic polarization testing in 0.5 M H_2SO_4 solution and electrochemical impedance spectroscopy (EIS), it is shown that adding Mo can effectively reduce the corrosion current density and improve the impedance of passive film, since the passivation layer is formed and stable.

Keywords: high-entropy alloys; body centered cubic; NiAl precipitates; high-temperature tensile; corrosion; EIS



Citation: Hsu, W.-C.; Kao, W.-P.; Yeh, J.-W.; Tsai, C.-W. Effect of Mo on the Mechanical and Corrosion Behaviors in Non-Equal Molar AlCrFeMnNi BCC High-Entropy Alloys. *Materials* **2022**, *15*, 751. <https://doi.org/10.3390/ma15030751>

Academic Editor: S. Joseph Poon

Received: 25 December 2021

Accepted: 15 January 2022

Published: 19 January 2022

Publisher's Note: MDPI stays neutral with regard to jurisdictional claims in published maps and institutional affiliations.



Copyright: © 2022 by the authors. Licensee MDPI, Basel, Switzerland. This article is an open access article distributed under the terms and conditions of the Creative Commons Attribution (CC BY) license (<https://creativecommons.org/licenses/by/4.0/>).

1. Introduction

In 2004, a new alloy design concept called high-entropy alloys (HEAs) was proposed by Yeh et al. [1–4]. In recent years, it has also been used in various research topics, including ceramics [5,6], polymers [7], and composites [8]. Unlike traditional alloys that are primarily based on one or two elements. HEAs comprise five or more principal elements in equimolar or non-equimolar ratios, each at 5–35 at%. The four core effects of HEAs, namely high entropy, lattice distortion, sluggish diffusion, and cocktail effects, mean that HEAs possess numerous special properties that traditional alloys do not. Besides, the idea of mixing multiple elements while increasing configurational entropy ($>1.5 R$) to enhance high-temperature phase stability expands the potential of new alloy design. Along with several extraordinary properties, HEAs have been applied to various functions and applications [9–13]. Moreover, the corrosion resistance [14–22] and mechanical properties [23–30] in HEAs are widely investigated due to their importance and necessity, and these fields have huge potential for further development. Nowadays, most research focuses on single-phase FCC alloys, such as CoCrFeMnNi [31,32] and CoCrFeNi [33,34], as well as BCC refractory alloys. Since the first report of MoNbTaVW alloys, research on BCC refractory HEAs has blossomed, with over 20 different HEA systems [35–42]. Nevertheless, to the authors' knowledge, the non-refractory BCC HEAs have been relatively overlooked from the mechanical point of view.

The $Al_xCrFe_{1.5}MnNi_{0.5}$ ($x = 0.3$ and 0.5) non-equimolar alloy based on the $Al_{0.5}CoCrCuFeNi$ [43–47] was demonstrated to be composed of FCC and BCC phase when Al content was 0.3 mole, and BCC phase when Al content was 0.5 mole [48]. Both displayed significant high-temperature age hardening ability, which resulted from the formation of ρ phase

(Cr₅Fe₆Mn₈-like phase) [48], and an extensive corrosion passive region [49,50]. Moreover, cobalt-free alloy design can largely reduce the cost and broaden the applications. However, these alloys present low processability and low corrosion resistance. It is shown that the corrosion current density of Al_xCrFe_{1.5}MnNi_{0.5} is two orders of magnitude higher than 304 stainless steel [49]. Therefore, the improvement of alloy composition design is necessary.

Mo is considered a beneficial element to both solid solution strengthening and precipitation hardening [51]. Mo-containing HEAs generally exhibited high strength [52], good thermal stability [53], and corrosion resistance [54–57]. Niu et al. mentioned that Mo-oxide film induced by appropriate Mo addition can enhance the corrosion resistance [56]. Although the effect of adding Mo on corrosion and mechanical properties has been widely discussed in FCC HEAs [54,56], there are few studies on the effects of Mo addition for the BCC HEAs. On the other hand, the content of Al in the alloy will affect the corrosion properties as well. Lee et al. pointed out that increasing the content of Al in Al_xCrFe_{1.5}MnNi_{0.5} ($x = 0, 0.3$ and 0.5) would raise the corrosion current density and passive current density [49]. The characteristics of the elements mentioned above will be taken into consideration in alloy design.

In the present study, the Co-free BCC Al_{0.4}CrFe_{1.5}MnNi_{0.5}Mo_x ($x = 0$ and 0.1) HEAs are investigated in order to maintain the single BCC matrix phase as well as enhance the corrosion resistance. The alloys will be prepared by reducing the Al content, and Mo addition can also improve the corrosion resistance [54–57]. With the examination of mechanical properties and corrosion resistance, a special focus is on the high-temperature tensile strength and corrosion current density. The electrochemical impedance spectroscopy (EIS) of these HEAs are also measured to observe the effect of Mo addition in the present alloys. In order to achieve industrial capacity, these properties would be a significant indicator.

2. Materials and Methods

The Al_{0.4}CrFe_{1.5}MnNi_{0.5}Mo_x ($x = 0$ and 0.1) alloys were prepared for analysis by vacuum arc melting. The purity of every element was a higher level above 99.9 wt%. Ingots with a weight of approximately 100 g were re-melted at least three times to make sure the chemical composition uniformity of the alloys. The ingots were 75 mm in length, 25 mm in width, and 10 mm in thickness. All ingots were forged at 1200 °C with a 50% thickness reduction, then homogenized at 1200 °C for 6 h followed by air cooling.

The crystal structures of the alloys were analyzed by X-ray diffraction (XRD, Bruker D2 PHASER). The X-ray source was a Cu target and the diffractometer worked at 30 kV/10 mA with a characteristic wavelength λ ($K_{\alpha 1}$) of 1.54056 Å. The angle of scanning ranged was from 20° to 100° and the scanning rate was 0.2°/s. The microstructures were obtained by scanning electron microscopy (SEM, JEOL JSM-IT100) operated at 20 kV. The chemical compositions were analyzed through energy dispersive X-ray spectroscopy (EDS). The SEM images of these alloys were taken without chemical etching. Thermo-Calc software was used to calculate the equilibrium phase as a function of temperature based on the CALPHAD method with the TCFE7 thermodynamic database. Tensile testing was performed with a universal testing system (SHIMADZU AGS-X 100 kN) equipped with a heating furnace (ATS series-3210) for temperature control. Flat dog-bone tensile specimens were electric discharge machined from the as-homogenized states with a gauge length of 19 mm, gauge width of 3.0 mm, and thickness of 1.5 mm. The engineering strain rate was 10^{-3} s^{-1} at elevated temperature. Each measurement was repeated three times for accuracy.

Both potentiodynamic polarization and electrochemical impedance spectroscopy (EIS) testing were conducted with a potentiostat (IVIUMnSTAT multichannel electrochemical analyzer) with a typical three electrode cell. An Hg/Hg₂Cl₂ electrode (saturated KCl) with $E = -0.2412 \text{ V}_{\text{SHE}}$ was used as the reference electrode and a platinum sheet was used as the counter electrode. The reacted surface area of $10 \times 10 \text{ mm}^2$ for all samples were ground to #1200 by SiC grit papers. The specimens were then tested in a 0.5 M H₂SO₄

solution at 25 °C under atmospheric pressure. The test solution was deaerated by bubbling purified nitrogen gas with the entire electrochemical tests to remove any effect of dissolved oxygen. In this case, it can be ensured that the electrochemical dissolution of the alloy is only contributed by the acidic solution (H_2SO_4). Potentiodynamic polarization curves and EIS were plotted after the specimen was allowed to corrode freely for 30 min, which is the time required to reach the quasi-steady-state value of open circuit potential (OCP). The potentiodynamic polarization tests were performed at a scan rate of 1 mV s^{-1} from an initial potential of -0.5 V to a final potential of 1.2 V versus to OCP. The EIS was conducted at OCP with a sinusoidal potential amplitude of 10 mV and an operating frequency of 100 kHz to 10 mHz . Following the potentiodynamic polarization and EIS testing, multiple electrochemical parameters were determined.

3. Results

3.1. Phase and Microstructure Analysis

Figure 1 shows the XRD patterns of the alloys in as-homogenized states. The crystal structures of the alloys all present a BCC solid solution structure. The lattice constants of $\text{Al}_{0.4}\text{CrFe}_{1.5}\text{MnNi}_{0.5}$ and $\text{Al}_{0.4}\text{CrFe}_{1.5}\text{MnNi}_{0.5}\text{Mo}_{0.1}$ are 2.885 \AA and 2.897 \AA , respectively. This result is consistent with the $\text{Al}_{0.5}\text{CrFe}_{1.5}\text{MnNi}_{0.5}$, which is a BCC solid solution structure in the previous study [48]. After adding Mo element, the increase in lattice constants is due to the contribution of Mo, whose radius is 141 p.m. [58], while the radii of the other elements except Al are approximately 125 p.m. [59]. Furthermore, it is noted that the (110) and (200) peak intensities of BCC phase in $\text{Al}_{0.4}\text{CrFe}_{1.5}\text{MnNi}_{0.5}\text{Mo}_{0.1}$ increase relative to $\text{Al}_{0.4}\text{CrFe}_{1.5}\text{MnNi}_{0.5}$. This indicates the increase in the degree of (110) and (200) texture after adding Mo element.

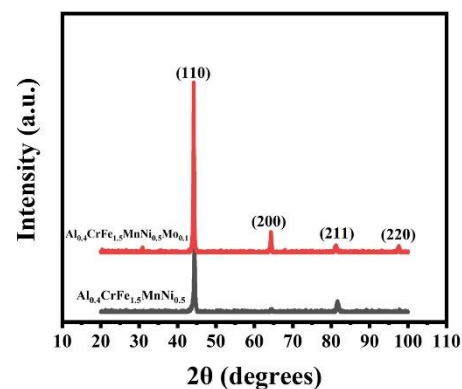


Figure 1. X-ray diffraction patterns of the alloys in as-homogenized state. Red: $\text{Al}_{0.4}\text{CrFe}_{1.5}\text{MnNi}_{0.5}\text{Mo}_{0.1}$; black: $\text{Al}_{0.4}\text{CrFe}_{1.5}\text{MnNi}_{0.5}$.

As shown in Figure 2a,b with low magnification, the obvious grains can be observed. No dendritic structure is found in alloys. The grain sizes of $\text{Al}_{0.4}\text{CrFe}_{1.5}\text{MnNi}_{0.5}$ and $\text{Al}_{0.4}\text{CrFe}_{1.5}\text{MnNi}_{0.5}\text{Mo}_{0.1}$ are $410 \pm 101 \mu\text{m}$ and $284 \pm 114 \mu\text{m}$ after 6 h homogenization, respectively. The grain size decreases from $410 \mu\text{m}$ to $284 \mu\text{m}$ are due to the addition of Mo. Since the melting temperature of Mo is 2896 K ($2623 \text{ }^\circ\text{C}$) and it is the highest one in this system, Mo can decrease the diffusion and form a refined crystal structure [60]. Figure 2c,d with high magnification indicate that both alloys have nano-scale precipitation in grains. According to previous studies [43,48], the fine gray precipitates in matrix are 7 nm to 50 nm and identified as the rich Al and Ni. In addition, Figure 3 shows that both alloys have a tendency of B2-type ordered phase formation before $1100 \text{ }^\circ\text{C}$ and single-phase BCC at $1200 \text{ }^\circ\text{C}$. The B2 structure is an ordered bcc structure including two simple cubic interpenetrating sublattices. Among these B2-based intermetallic compounds, the most common compound is NiAl. A comparison with Figure 2c,d indicates that even though the two alloys underwent heat treatment at $1200 \text{ }^\circ\text{C}$, they are still not single-phase. It can be concluded that the precipitates are thus a solution phase of the NiAl compound with

ordered BCC (B2-type), where there were elemental replacement. In other words, Fe and Mn for partial Ni, and Cr for partial Al. From a high magnification microstructure, the precipitate size of Figure 2e is 43 nm, and the size of Figure 2f is 26 nm. It can be inferred that adding Mo also reduced the particle size, which may be due to the slow grain growth of the samples.

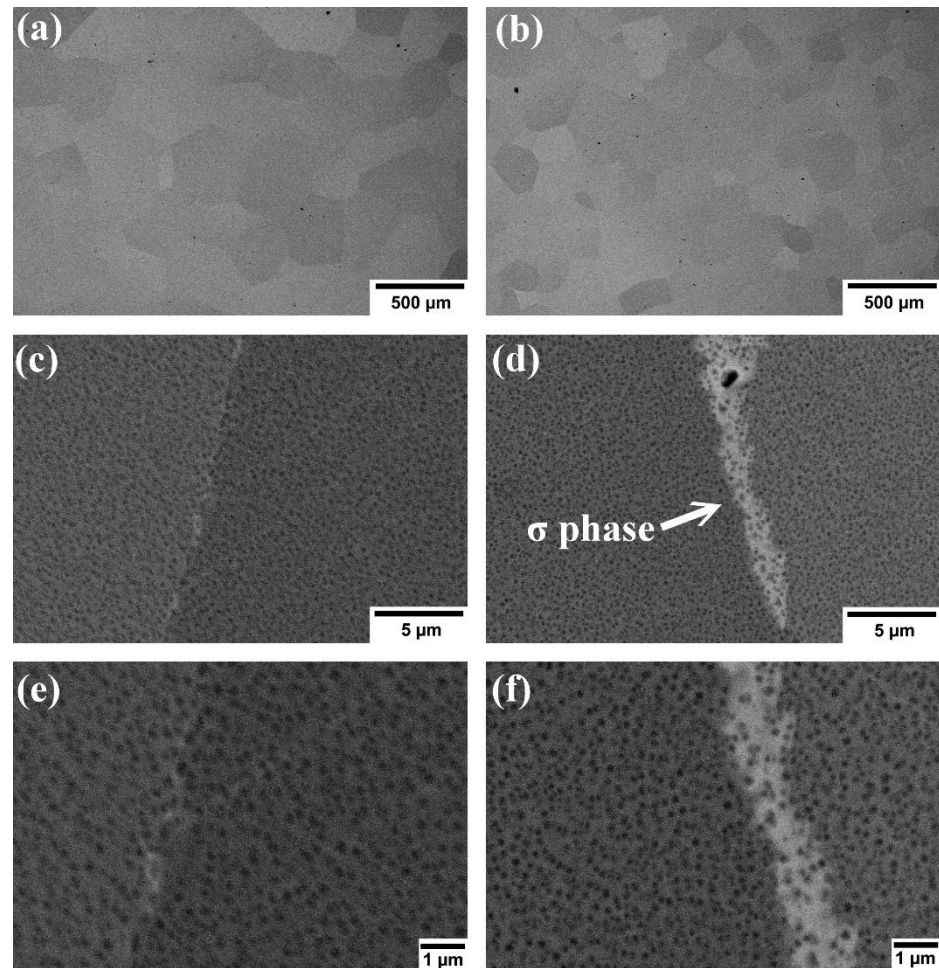


Figure 2. Microstructure of alloys: (a,c,e) are $\text{Al}_{0.4}\text{CrFe}_{1.5}\text{MnNi}_{0.5}$, and (b,d,f) $\text{Al}_{0.4}\text{CrFe}_{1.5}\text{MnNi}_{0.5}\text{Mo}_{0.1}$ in backscatter electron images. Below is the high magnification surface of the specimens.

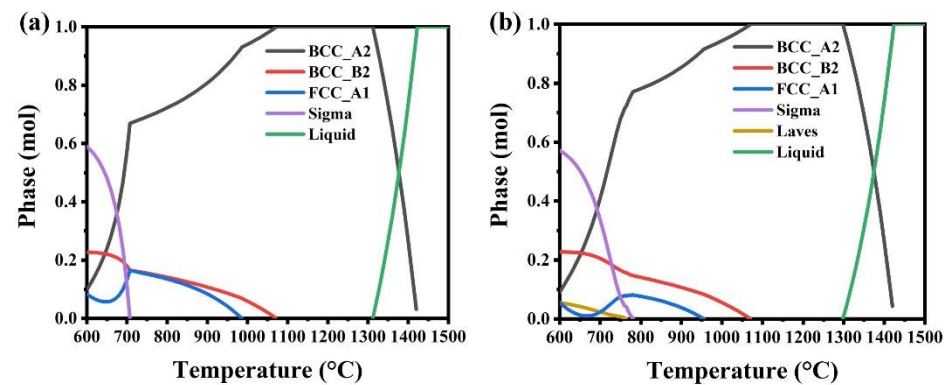


Figure 3. Thermo-Calc calculation diagrams, calculated using the CALPHAD method with the TCFe7 database, for (a) $\text{Al}_{0.4}\text{CrFe}_{1.5}\text{MnNi}_{0.5}$ and (b) $\text{Al}_{0.4}\text{CrFe}_{1.5}\text{MnNi}_{0.5}\text{Mo}_{0.1}$.

The microstructure in Figure 2d shows white phase on the grain boundary, indicating that $\text{Al}_{0.4}\text{CrFe}_{1.5}\text{MnNi}_{0.5}\text{Mo}_{0.1}$ alloy has composition segregation on the grain boundary. According to Table 1, the white region along grain boundaries in $\text{Al}_{0.4}\text{CrFe}_{1.5}\text{MnNi}_{0.5}\text{Mo}_{0.1}$ alloy has higher Cr and Mo contents and a lower Ni content than the gray phase region, which is known to be the σ phase [61,62]. The σ phase is mostly found in the iron-chromium-molybdenum system. Its crystal structure is defined as the topologically close-packed (TCP) phase, which is observed in many intermetallic compounds. However, it can be found in Figure 3b that the σ phase cannot form above 800 °C. This contradiction is owing to hot forged behavior which was led mainly by dynamic recrystallization [63]. There are more heterogeneous nucleation sites such as grain boundaries, so the complex σ phase is difficult to completely melt back into the matrix. Moreover, the σ phase formation tendency of austenitic stainless steel can be known from the equivalent chromium content (ECC) equation in weight percent [64]:

$$\begin{aligned} \text{ECC} = & \% \text{ chromium (Cr)} + 0.31\% \text{ manganese (Mn)} \\ & + 1.76\% \text{ molybdenum (Mo)} + 0.97\% \text{ tungsten (W)} \\ & + 2.02\% \text{ vanadium (V)} + 1.58\% \text{ silicon (Si)} \\ & + 2.44\% \text{ titanium (Ti)} + 1.7\% \text{ niobium (Nb)} \\ & + 1.22\% \text{ tantalum (Ta)} - 0.226\% \text{ nickel (Ni)} \\ & - 0.177\% \text{ cobalt (Co)} \end{aligned} \quad (1)$$

If the ECC is greater than 17–18%, the steel tends to form σ phase. In this case, the ECC value for the $\text{Al}_{0.4}\text{CrFe}_{1.5}\text{MnNi}_{0.5}\text{Mo}_{0.1}$ alloy was 32.8%. This indicates that the formation of σ phase in the Mo-containing alloy is reasonable.

Table 1. Chemical compositions from EDS analysis of the alloys (unit: at.%).

Alloys	Elements	Al	Cr	Fe	Mn	Ni	Mo
$\text{Al}_{0.4}\text{CrFe}_{1.5}\text{MnNi}_{0.5}$	matrix	9.1 ± 0.6	23.7 ± 0.2	32.2 ± 0.6	23.8 ± 0.4	11.1 ± 0.1	-
	matrix	8.4 ± 0.5	22.5 ± 0.5	31.7 ± 0.4	24.9 ± 0.4	10.2 ± 0.2	2.3 ± 0.2
$\text{Al}_{0.4}\text{CrFe}_{1.5}\text{MnNi}_{0.5}\text{Mo}_{0.1}$	Gray	8.9 ± 0.3	23.6 ± 0.5	34.7 ± 0.2	20.8 ± 0.4	9.4 ± 0.3	2.6 ± 0.2
	White	7.8 ± 0.4	24.8 ± 0.3	34.3 ± 0.1	22.2 ± 0.2	7.76 ± 0.4	3.15 ± 0.1

3.2. High-Temperature Tensile Results

Since both the alloys demonstrate excellent hardening ability, the mechanical properties of the $\text{Al}_{0.4}\text{CrFe}_{1.5}\text{MnNi}_{0.5}$ and the $\text{Al}_{0.4}\text{CrFe}_{1.5}\text{MnNi}_{0.5}\text{Mo}_{0.1}$ at high-temperature were examined. Figure 4 shows the engineering tensile stress-strain curves at 600 °C. The yield strength of the $\text{Al}_{0.4}\text{CrFe}_{1.5}\text{MnNi}_{0.5}$ is above 300 MPa and the $\text{Al}_{0.4}\text{CrFe}_{1.5}\text{MnNi}_{0.5}\text{Mo}_{0.1}$ exceeds 400 MPa even at 600 °C. The yield strength (YS), ultimate tensile strength (UTS), and elongation (EL) of the alloys are listed in Table 2. The volume fraction of the B2-type NiAl precipitate is higher than 30%, and it can sustain high strength at high-temperature. Meanwhile, the $\text{Al}_{0.4}\text{CrFe}_{1.5}\text{MnNi}_{0.5}\text{Mo}_{0.1}$ shows higher yield strength than the $\text{Al}_{0.4}\text{CrFe}_{1.5}\text{MnNi}_{0.5}$, and this is due to the precipitation hardening by σ phase. Moreover, both the alloys demonstrate the best ductility at 600 °C, especially $\text{Al}_{0.4}\text{CrFe}_{1.5}\text{MnNi}_{0.5}$, at up to 32%. These results indicate that the $\text{Al}_{0.4}\text{CrFe}_{1.5}\text{MnNi}_{0.5}$ and the $\text{Al}_{0.4}\text{CrFe}_{1.5}\text{MnNi}_{0.5}\text{Mo}_{0.1}$ show a good strength–ductility balance at elevated temperature. The mechanisms of high-temperature strength and ductility will be discussed in detail later.

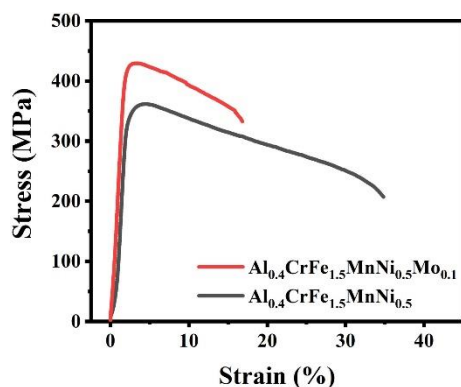


Figure 4. Tensile engineering stress-strain curve of $\text{Al}_{0.4}\text{CrFe}_{1.5}\text{MnNi}_{0.5}$ and $\text{Al}_{0.4}\text{CrFe}_{1.5}\text{MnNi}_{0.5}\text{Mo}_{0.1}$ alloys at 600 °C.

Table 2. The YS, UTS, and EL of the alloys at 600 °C.

Alloys	YS (MPa)	UTS (MPa)	EL (%)
$\text{Al}_{0.4}\text{CrFe}_{1.5}\text{MnNi}_{0.5}$	307	361	32.7
$\text{Al}_{0.4}\text{CrFe}_{1.5}\text{MnNi}_{0.5}\text{Mo}_{0.1}$	413	430	14.7

Figure 5 shows the fracture surface of both alloys after tensile tests at 600 °C. The fracture surface of $\text{Al}_{0.4}\text{CrFe}_{1.5}\text{MnNi}_{0.5}$ alloy shows a 45 degree fracture, indicating that a ductile rupture was formed, as shown in Figure 5a. In addition, the fracture surface under micro view exhibited many ductile dimples, as shown in Figure 5c,e. This further confirms that $\text{Al}_{0.4}\text{CrFe}_{1.5}\text{MnNi}_{0.5}$ alloy is a typical ductile fracture. On the other hand, Figure 5b illustrates the flat fracture surface of $\text{Al}_{0.4}\text{CrFe}_{1.5}\text{MnNi}_{0.5}\text{Mo}_{0.1}$ alloy. The obvious intergranular fracture owing to the brittle σ phase precipitation along grain boundaries can be found, as shown in Figure 5d. Besides, the typical brittle fracture pattern is directly related to the brittle σ phase precipitated in $\text{Al}_{0.4}\text{CrFe}_{1.5}\text{MnNi}_{0.5}\text{Mo}_{0.1}$ alloy, as shown in Figure 5f. However, Figure 5d shows the microridge structures (white arrow) formed on the grains, revealing local ductility in the alloy. So, $\text{Al}_{0.4}\text{CrFe}_{1.5}\text{MnNi}_{0.5}\text{Mo}_{0.1}$ alloy is still provided with a slightly ductile instead of completely brittle fracture.

3.3. Electrochemical Properties Analysis

Figure 6 plots the potentiodynamic polarization curves of the alloys in 0.5 M H_2SO_4 solution. All alloys present a typical passive region. Table 3 summarizes the values of electrochemical parameters for the alloys in 0.5 M H_2SO_4 solution. The corrosion current densities (I_{corr}) of the $\text{Al}_{0.4}\text{CrFe}_{1.5}\text{MnNi}_{0.5}\text{Mo}_x$ alloy are determined to fall from 3200 $\mu\text{A}/\text{cm}^2$ to 61 $\mu\text{A}/\text{cm}^2$ as the Mo content increased to 0.1 mol. The corrosion potentials (E_{corr}) of $\text{Al}_{0.4}\text{CrFe}_{1.5}\text{MnNi}_{0.5}$ and $\text{Al}_{0.4}\text{CrFe}_{1.5}\text{MnNi}_{0.5}\text{Mo}_{0.1}$ are −340 and −60 mV, respectively. Based on the above results, the addition of 0.1 mol Mo can inhibit the reduction reaction of hydrogen ions in the solution and greatly increase the corrosion resistance. Furthermore, the critical current density (I_{crit}) would drastically drop from 1.1×10^{-2} A/cm^2 to 2.7×10^{-4} A/cm^2 when the alloy is supplemented with Mo, implying that $\text{Al}_{0.4}\text{CrFe}_{1.5}\text{MnNi}_{0.5}$ faces a greater obstacle before entering passivation. Critical pitting potential (E_{pit}) is the minimum positive potential at which the metal salt of the aggressive ion in solution is in equilibrium with the metal oxide. All alloys present similar values of E_{pit} . This is due to the continuous increase of applied potential, and the release of oxygen after reaching the electrolysis potential of water (1.23V) becomes the main reaction mechanism. In addition, the potentiodynamic polarization curve shows that the $\text{Al}_{0.4}\text{CrFe}_{1.5}\text{MnNi}_{0.5}\text{Mo}_{0.1}$ has a negative and large hysteresis loop, which means that the metal is still well protected after passivation.

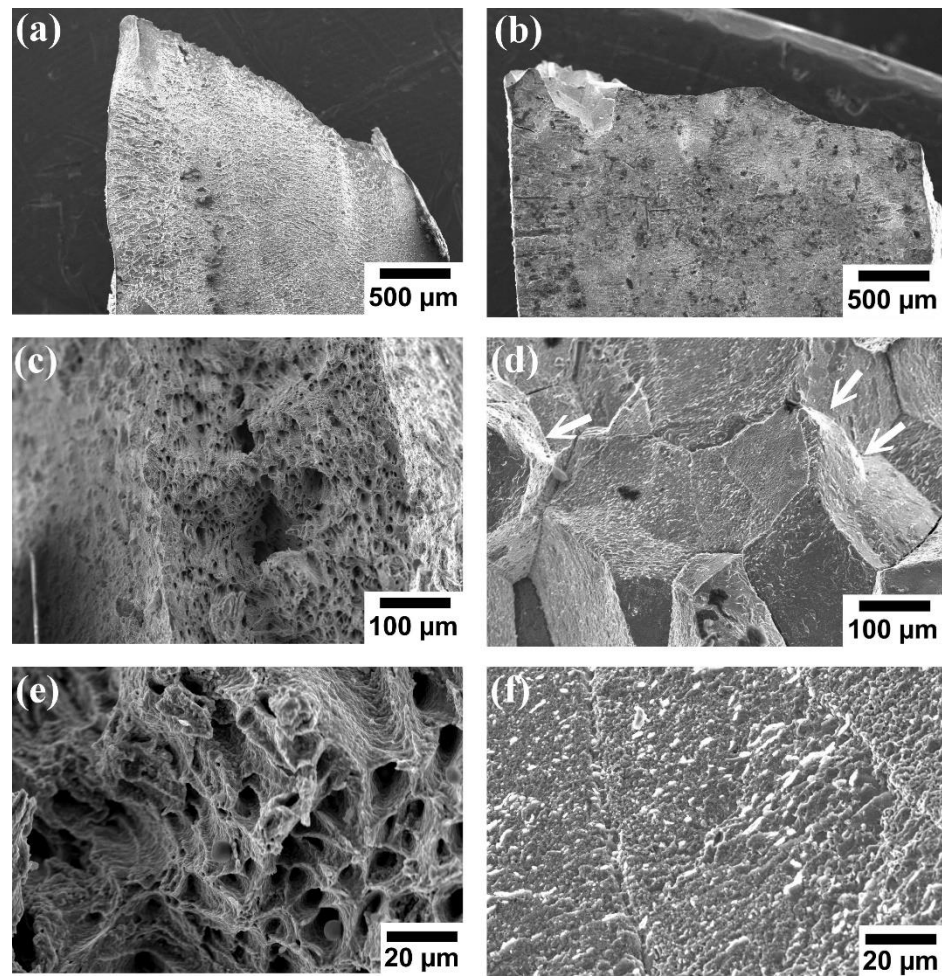


Figure 5. Fractography of $\text{Al}_{0.4}\text{CrFe}_{1.5}\text{MnNi}_{0.5}\text{Mo}_x$ alloys: (a,c,e) $x = 0$ and (b,d,f) $x = 0.1$. Below is the high magnification surface of the specimens. The white arrows are the positions of the microridge structures.

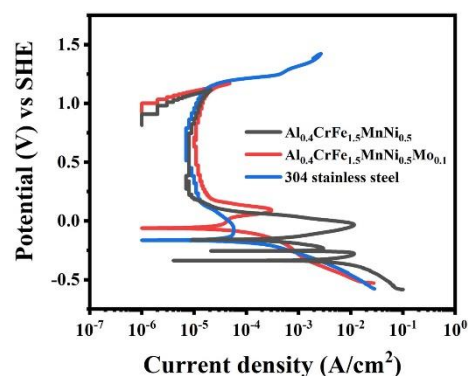


Figure 6. Potentiodynamic polarization curves of the alloys in 0.5 M H_2SO_4 solution.

To further investigate the interface of the corrosion reaction between solution and alloys, the electrochemical impedance spectroscopy test of the alloys in 0.5 M H_2SO_4 solution are shown in Figure 7. The Nyquist plot of the $\text{Al}_{0.4}\text{CrFe}_{1.5}\text{MnNi}_{0.5}\text{Mo}_{0.1}$ and 304 stainless steel alloys include one capacitive loop from high to low frequencies, revealing that the alloys are provided with a passivation layer when corroded. $\text{Al}_{0.4}\text{CrFe}_{1.5}\text{MnNi}_{0.5}\text{Mo}_{0.1}$ alloys only include one capacitive loop, resulting from the presence of Mo element in HEA. This element is present in the outer regions of the passive film as Mo(VI) and generates

in its unoxidized state at the metallic matrix immediately beneath the film, which can be used as a barrier and inhibit the formation of adsorption layer [57]. On the other hand, a different behavior was observed in $\text{Al}_{0.4}\text{CrFe}_{1.5}\text{MnNi}_{0.5}$ alloy. It includes two capacitive loops in electrochemical impedance diagrams, which are typically related to the presence of a passivation layer and an adsorption layer. The reason for the formation of the adsorption layer is that the elements, such as Al, Cr, and Ni, in the alloy dissolve in the solution, forming compounds with hydroxide or sulfate ions and adsorbing on the metal surface, thus forming the adsorption layer [65,66].

Table 3. E_{corr} , I_{corr} , I_{pass} , and E_{pit} of the alloys in 0.5 M H_2SO_4 solution.

Alloys	I_{corr} ($\mu\text{A}/\text{cm}^2$)	E_{corr} (mV _{SHE})	I_{crit} ($\mu\text{A}/\text{cm}^2$)	I_{pass} ($\mu\text{A}/\text{cm}^2$)	E_{pit} (mV _{SHE})
$\text{Al}_{0.4}\text{CrFe}_{1.5}\text{MnNi}_{0.5}$	3200	−340	11,000	8	1120
$\text{Al}_{0.4}\text{CrFe}_{1.5}\text{MnNi}_{0.5}\text{Mo}_{0.1}$	61	−60	270	10	1120
304 stainless steel	72	−160	58	7	1150

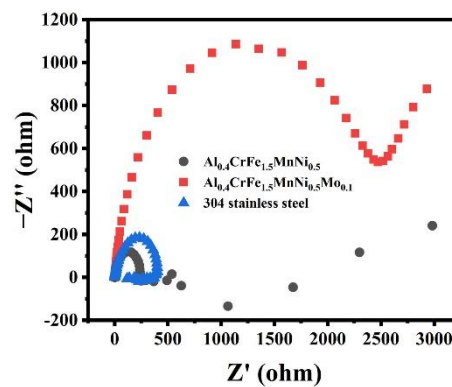


Figure 7. Nyquist plot of the alloys in 0.5 M H_2SO_4 solution.

Figure 8 presents the Bode plots of the alloys. Similar to the previous results, the phase in Figure 8a has two peaks and the impedance changes significantly at low frequencies, indicating that two layers are produced in $\text{Al}_{0.4}\text{CrFe}_{1.5}\text{MnNi}_{0.5}$ alloy. The other two alloys have one phase peak as shown in Figure 8b,c, which means that only one passivation layer is formed. Moreover, Table 4 summarizes the simulated values for the equivalent circuit elements. R_s is the resistance of the solution; R_{pass} is the charge transfer resistance that is associated with the protection ability of passivation layer; R_{ad} represents the resistance of the adsorptive film on the metal surface, while Q_{pass} and Q_{ad} are the capacitance of passive layer constant phase element and the capacitance of adsorptive film constant phase element, respectively. Based on above results, the impedance value of the passive layer (R_{pass}) of $\text{Al}_{0.4}\text{CrFe}_{1.5}\text{MnNi}_{0.5}\text{Mo}_{0.1}$ is much greater than $\text{Al}_{0.4}\text{CrFe}_{1.5}\text{MnNi}_{0.5}$ and 304 stainless steel during passivation, showing that the passivation layer of $\text{Al}_{0.4}\text{CrFe}_{1.5}\text{MnNi}_{0.5}\text{Mo}_{0.1}$ possesses better protection ability. To sum up, the corrosion current density and corrosion potential of $\text{Al}_{0.4}\text{CrFe}_{1.5}\text{MnNi}_{0.5}\text{Mo}_{0.1}$ in 0.5 M H_2SO_4 are better than those of $\text{Al}_{0.4}\text{CrFe}_{1.5}\text{MnNi}_{0.5}$ and 304 stainless steel alloys. Furthermore, the impedance of the $\text{Al}_{0.4}\text{CrFe}_{1.5}\text{MnNi}_{0.5}\text{Mo}_{0.1}$ passivation layer is the largest, indicating that its corrosion resistance is the best in three alloys.

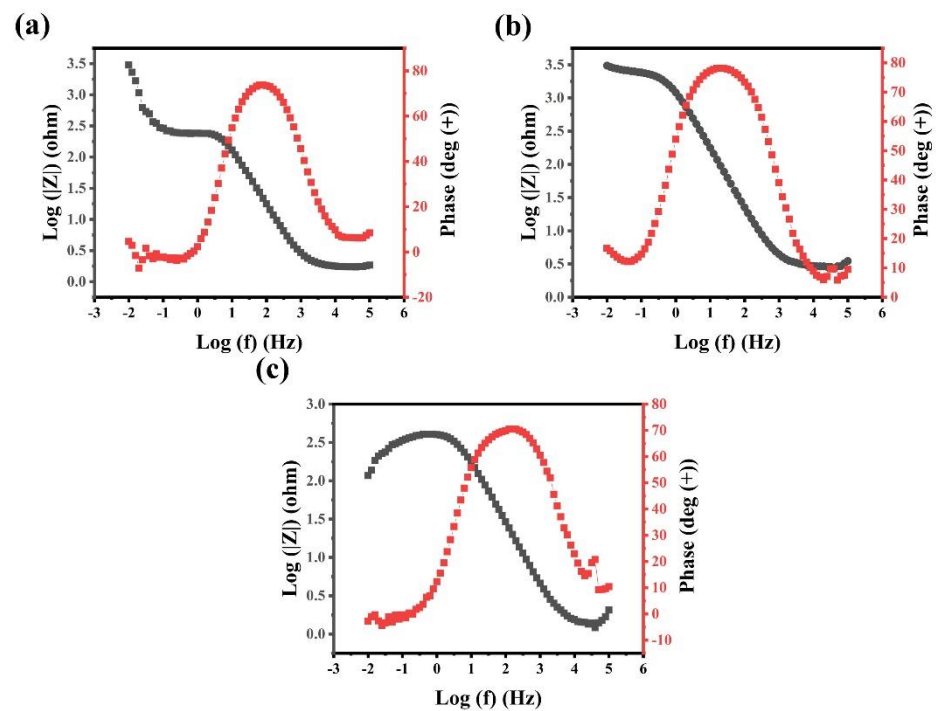


Figure 8. Bode plot of (a) $\text{Al}_{0.4}\text{CrFe}_{1.5}\text{MnNi}_{0.5}$ (b) $\text{Al}_{0.4}\text{CrFe}_{1.5}\text{MnNi}_{0.5}\text{Mo}_{0.1}$ (c) 304 stainless steel in 0.5 M H_2SO_4 solution.

Table 4. Equivalent circuit elements values for EIS data corresponding to the alloys in 0.5 M H_2SO_4 solution.

Alloys	R_s (ohm)	R_{pass} (ohm)	Q_{pass} ($\mu\text{S}\cdot\text{s}^n/\text{cm}^2$)	R_{ad} (ohm)	Q_{ad} ($\mu\text{S}\cdot\text{s}^n/\text{cm}^2$)
$\text{Al}_{0.4}\text{CrFe}_{1.5}\text{MnNi}_{0.5}$	1.8	30.8	72.9	233.9	33.4
$\text{Al}_{0.4}\text{CrFe}_{1.5}\text{MnNi}_{0.5}\text{Mo}_{0.1}$	2.9	2348	127	-	-
304 stainless steel	1.4	252.7	115.5	-	-

4. Discussion

4.1. Elongation Behavior of the Alloys at High-Temperature

Both alloys cracked within 5% of rolling at room temperature and showed the characteristics of a complete brittle fracture (not shown here). However, as shown in Figure 5c,e, the ductile fracture mode, such as dimples and microvoids, can be seen on the fracture surface of the alloys. Moreover, their elongation is greatly increased at 600 °C, especially $\text{Al}_{0.4}\text{CrFe}_{1.5}\text{MnNi}_{0.5}$ alloy. The reason for the increase in elongation is that the alloys experience brittle to ductile transition at high-temperature. In BCC HEAs, the Peierls–Nabarro stress is expected to be very high because the slip plane consists of different atoms with different sizes, which may increase the lattice resistance to the movement of dislocations [67].

The nucleation and propagation of double kink is a mechanism to overcome lattice resistance through the motion of $a/2 \langle 111 \rangle$ screw dislocation in bcc metals [68]. Kink will ease the movement of dislocations through the lattice. Since the kinked sections are located across higher energy portions of the crystal, they can slip more simply than the line segment along the energy troughs, which must overcome the largest energy barrier if they move. However, kink formation is a thermally activated process [69], which implies that at high-temperature the number of double kinks is just enough to let dislocation slip [70]. Hence, the elongation of the both alloys is increased substantially at high-temperature.

4.2. Effects of the NiAl Precipitates and σ Phase on Deformation Behavior at High-Temperature

According to a previous study [48], the $\text{Al}_x\text{CrFe}_{1.5}\text{MnNi}_{0.5}$ ($x = 0.3$ and 0.5) series alloy exhibits a large age hardening effect at temperatures from 600 to 800 °C. For instance, the hardness of both alloys increases from Hv 300 to Hv 550 in 1 h. The aging hardening ability is due to the formation of ρ phase ($\text{Cr}_5\text{Fe}_6\text{Mn}_8$ -like phase), which displays a very high hardness of Hv 1273. However, the hardness of the alloys in this study falls between 350 and 400 HV whether the alloys have undergone tensile testing at 600 °C. It can be inferred that the ρ phase is not formed during tensile testing, and there is no strengthening contribution of the ρ phase.

On the other hand, as shown in Figure 2b,d, both alloys disperse with nano B2-type NiAl precipitates in the matrix. Fine NiAl precipitates with diameters of 10–30 nm were found to significantly strengthen the Fe-Al-Ni-based alloy, which is because of the difference primary slip system between the BCC matrix and the B2 precipitates [71]. The nano-scale NiAl precipitates can also be found in HEAs resulting in improved mechanical properties [72,73]. Generally, the $\{101\} \langle 111 \rangle$ slip occurs in BCC metals while B2 crystals are known to deform by $\{110\} \langle 001 \rangle$ slip at room temperature [74]. The activation of $\langle 111 \rangle$ slip unfavorable for the NiAl precipitates leads to great hardening ability during tensile testing, called slip frustration hardening (SFH) [75]. However, the slip system changes from $\langle 111 \rangle$ to $\langle 001 \rangle$ at 650 °C because the critical resolved shear stress for $\langle 001 \rangle$ slip of the B2 crystals drop rapidly with increasing temperature [76]. This means that the NiAl precipitates are sheared by $\langle 001 \rangle$ dislocations and bypassed by the $1/2 \langle 111 \rangle$ dislocations, resulting in the strengthening of alloys by both SFH and the Orowan strengthening at elevated temperature [75]. As a result, alloys containing B2-type NiAl precipitates and BCC matrix exhibit excellent elevated mechanical strength. Further experiments are required to confirm the formation of the slip system and dislocation movement in $\text{Al}_{0.4}\text{CrFe}_{1.5}\text{MnNi}_{0.5}\text{Mo}_x$ ($x = 0$ and 0.1) alloys.

$\text{Al}_{0.4}\text{CrFe}_{1.5}\text{MnNi}_{0.5}\text{Mo}_{0.1}$ had a hardness of about 30HV lower than $\text{Al}_{0.4}\text{CrFe}_{1.5}\text{MnNi}_{0.5}$, but it exhibited better yield strength (YS) and ultimate tensile strength (UTS) at high-temperature. Since the σ phase was harder, it could be used as an obstacle to dislocation when stretched. Wang et al. [77] stated that the harder σ phase could hinder the dislocation movement during the tensile process and finally enhance the strength of duplex stainless steel, but the elongation would decrease. Zhang et al. [78] also reported that the low volume fraction of the nano- σ particles in FCC HEAs can strengthen the alloy with less sacrifice of ductility. Therefore, the $\text{Al}_{0.4}\text{CrFe}_{1.5}\text{MnNi}_{0.5}\text{Mo}_{0.1}$ alloy possesses better mechanical strength without sacrificing lots of ductility.

4.3. Effects of Mo Addition on the Corrosion Behavior

The beneficial effects of adding Mo are widely recognized with regard to the corrosion resistance of stainless steel [79–81]. Sugimoto and Sawada [82] stated that the addition of Mo to austenitic stainless steel can form a passive film composed of a solid solution of Mo^{6+} in a chromium oxyhydroxide network, which drops the corrosion current density in the active region for acidic solution. However, Hashimoto et al. [83] proposed that the main role of Mo is to reduce the dissolution rate of the active zones by forming and retaining Mo (VI) oxyhydroxide or molybdate (MoO_4^{2-}) at these positions.

As mentioned above, many authors conclude that molybdenum in the passivation layer is primarily an ionic compound (MoO_4^{2-}) that adsorbs on top of the material surface and acts as a barrier to electrochemical attack [81,84,85]. However, given the strong acidic conditions ($\text{pH} < 1$) and the corrosion potential of the materials in the present studied solution, the influence of Mo through molybdate formation should be considered impossible according to the Pourbaix diagrams [86]. Since molybdate is thermodynamically unstable, it tends to precipitate as MoO_3 oxide under these conditions. MoO_3 is a protective oxide layer, which can decrease the rate of the corrosion process, leading to an improvement in the corrosion behavior in H_2SO_4 solution. Hence, $\text{Al}_{0.4}\text{CrFe}_{1.5}\text{MnNi}_{0.5}\text{Mo}_{0.1}$ alloy possesses

better corrosion resistance than $\text{Al}_{0.4}\text{CrFe}_{1.5}\text{MnNi}_{0.5}$ alloy owing to the MoO_3 protective oxide layer.

5. Conclusions

Adding Mo to the $\text{Al}_{0.4}\text{CrFe}_{1.5}\text{MnNi}_{0.5}\text{Mo}_x$ ($x = 0$ and 0.1) alloy strengthens with σ phase. The body-centered cubic (bcc) high-entropy alloys (HEAs) improved the elevated mechanical property and corrosion property at the same time.

1. The present alloys are all BCC solid-solution structures and disperse with the nano B2-type NiAl precipitates in the matrix. Moreover, $\text{Al}_{0.4}\text{CrFe}_{1.5}\text{MnNi}_{0.5}\text{Mo}_{0.1}$ exists as σ phase with rich Cr and Mo contents and a lack of Ni content along the grain boundary.
2. The mechanical properties of the alloys improve upon Mo addition, reaching a yield strength of 413 MPa, an ultimate tensile strength of 430 MPa, and an elongation of 14.7% at 600 °C. This is ascribed to the slip frustration hardening (SFH) of nano NiAl precipitates and the precipitation hardening of σ phase. The results indicate that $\text{Al}_{0.4}\text{CrFe}_{1.5}\text{MnNi}_{0.5}\text{Mo}_{0.1}$ shows good strength–ductility balance at elevated temperature.
3. $\text{Al}_{0.4}\text{CrFe}_{1.5}\text{MnNi}_{0.5}\text{Mo}_{0.1}$ alloy exhibits superior corrosion resistance compared to $\text{Al}_{0.4}\text{CrFe}_{1.5}\text{MnNi}_{0.5}$ and 304 stainless steel. In addition, the impedance of the $\text{Al}_{0.4}\text{CrFe}_{1.5}\text{MnNi}_{0.5}\text{Mo}_{0.1}$ passivation layer is the largest, indicating that its passive film is formed and stable. The results agree with the formation of the MoO_3 protective layer. Therefore, we can conclude that Mo addition improves the corrosion resistance of HEAs.

Author Contributions: Conceptualization, W.-C.H.; methodology, W.-C.H. and W.-P.K.; formal analysis, W.-C.H.; investigation, W.-C.H. and W.-P.K.; data curation, W.-C.H.; writing—original draft preparation, W.-C.H.; writing—review and editing, W.-C.H.; visualization, W.-C.H., W.-P.K., J.-W.Y. and C.-W.T.; supervision, J.-W.Y. and C.-W.T.; project administration, J.-W.Y. and C.-W.T. All authors have read and agreed to the published version of the manuscript.

Funding: This research received no external funding.

Institutional Review Board Statement: Not applicable.

Informed Consent Statement: Not applicable.

Data Availability Statement: The data presented in this study are available on request from the corresponding author and data is contained within the article.

Acknowledgments: This work was financially supported by the “High Entropy Materials Center” from The Featured Areas Research Center Program within the framework of the Higher Education Sprout Project by the Ministry of Education (MOE) and from the Project MOST 110-2634-F-007-024 and 110-2224-E-007-001 by Ministry of Science and Technology (MOST) in Taiwan.

Conflicts of Interest: The authors declare no conflict of interest.

References

1. Yeh, J.-W.; Chen, S.K.; Lin, S.-J.; Gan, J.-Y.; Chin, T.-S.; Shun, T.-T.; Tsau, C.-H.; Chang, S.-Y. Nanostructured high-entropy alloys with multiple principal elements: Novel alloy design concepts and outcomes. *Adv. Eng. Mater.* **2004**, *6*, 299–303. [[CrossRef](#)]
2. Jien-Wei, Y. Recent progress in high entropy alloys. *Ann. Chim. Sci. Mat.* **2006**, *31*, 633–648.
3. Yeh, J.-W. Alloy design strategies and future trends in high-entropy alloys. *JOM* **2013**, *65*, 1759–1771. [[CrossRef](#)]
4. Miracle, D.B.; Senkov, O.N. A critical review of high entropy alloys and related concepts. *Acta Mater.* **2017**, *122*, 448–511. [[CrossRef](#)]
5. Chen, T.-Y.; Wang, S.Y.; Kuo, C.H.; Huang, S.C.; Lin, M.H.; Li, C.H.; Chen, H.Y. In operando synchrotron X-ray studies of a novel spinel (Ni 0.2 Co 0.2 Mn 0.2 Fe 0.2 Ti 0.2) 3 O 4 high-entropy oxide for energy storage applications. *J. Mater. Chem. A* **2020**, *8*, 21756–21770. [[CrossRef](#)]
6. Chen, T.; Shun, T.T.; Yeh, J.W.; Wong, M.S. Nanostructured nitride films of multi-element high-entropy alloys by reactive DC sputtering. *Surf. Coat. Technol.* **2004**, *188*, 193–200. [[CrossRef](#)]

7. Huang, Y.-J.; Yeh, J.-W.; Yang, A.C.-M. High-entropy polymers: A new route of polymer mixing with suppressed phase separation. *Materialia* **2021**, *15*, 100978. [[CrossRef](#)]
8. Peng, C.-H.; Tsai, C.-W.; Kuo, C.-M.; Chiu, S.-M. High-temperature tribological behavior of Al_{0.3}Cr_{0.5}Fe_{1.5}Mn_{0.5}Ni high-entropy alloys with addition of titanium and carbon. *Front. Mater.* **2022**, *8*, 508. [[CrossRef](#)]
9. Liu, H.-C.; Tsai, C.-W. Effect of Ge addition on the microstructure, mechanical properties, and corrosion behavior of CoCrFeNi high-entropy alloys. *Intermetallics* **2021**, *132*, 107167. [[CrossRef](#)]
10. Lin, P.-T.; Liu, H.-C.; Hsieh, P.-Y.; Wei, C.-Y.; Tsai, C.-W.; Sato, Y.S.; Chen, S.-C.; Yen, H.-W.; Lu, N.-H.; Chen, C.-H. Heterogeneous structure-induced strength-ductility synergy by partial recrystallization during friction stir welding of a high-entropy alloy. *Mater. Des.* **2021**, *197*, 109238. [[CrossRef](#)]
11. Chang, S.-H.; Kao, W.-P.; Hsiao, K.-Y.; Yeh, J.-W.; Lu, M.-Y.; Tsai, C.-W. High-temperature shape memory properties of Cu₁₅Ni₃₅Ti₂₅Hf_{12.5}Zr_{12.5} high-entropy alloy. *J. Mater. Res. Technol.* **2021**, *14*, 1235–1242. [[CrossRef](#)]
12. Yang, J.-J.; Kuo, C.-M.; Lin, P.-T.; Liu, H.-C.; Huang, C.-Y.; Yen, H.-W.; Tsai, C.-W. Improvement in oxidation behavior of Al_{0.2}Co_{1.5}CrFeNi_{1.5}Ti_{0.3} high-entropy superalloys by minor Nb addition. *J. Alloys Compd.* **2020**, *825*, 153983. [[CrossRef](#)]
13. Hsu, C.-Y.; Juan, C.-C.; Wang, W.-R.; Sheu, T.-S.; Yeh, J.-W.; Chen, S.-K. On the superior hot hardness and softening resistance of AlCoCrFeMo_{0.5}Ni high-entropy alloys. *Mater. Sci. Eng. A* **2011**, *528*, 3581–3588. [[CrossRef](#)]
14. Liang, H.-L.; Tsai, C.-W.; Guo, S. Design of corrosion-resistant high-entropy alloys through valence electron concentration and new PHACOMP. *J. Alloys Compd.* **2021**, *883*, 160787. [[CrossRef](#)]
15. Tang, Z.; Huang, L.; He, W.; Liaw, P.K. Alloying and processing effects on the aqueous corrosion behavior of high-entropy alloys. *Entropy* **2014**, *16*, 895–911. [[CrossRef](#)]
16. Qiu, X.-W.; Wu, M.-J.; Liu, C.-G.; Zhang, Y.-P.; Huang, C.-X. Corrosion performance of Al₂CrFeCoxCuNiTi high-entropy alloy coatings in acid liquids. *J. Alloys Compd.* **2017**, *708*, 353–357. [[CrossRef](#)]
17. Nair, R.; Arora, H.; Mukherjee, S.; Singh, S.; Singh, H.; Grewal, H. Exceptionally high cavitation erosion and corrosion resistance of a high entropy alloy. *Ultrason. Sonochemistry* **2017**, *41*, 252–260. [[CrossRef](#)] [[PubMed](#)]
18. Shi, Y.; Collins, L.; Feng, R.; Zhang, C.; Balke, N.; Liaw, P.K.; Yang, B. Homogenization of Al_xCoCrFeNi high-entropy alloys with improved corrosion resistance. *Corros. Sci.* **2018**, *133*, 120–131. [[CrossRef](#)]
19. Shi, Y.; Collins, L.; Balke, N.; Liaw, P.K.; Yang, B. In-situ electrochemical-AFM study of localized corrosion of Al_xCoCrFeNi high-entropy alloys in chloride solution. *Appl. Surf. Sci.* **2018**, *439*, 533–544. [[CrossRef](#)]
20. Chen, Y.; Duval, T.; Hung, U.; Yeh, J.; Shih, H. Microstructure and electrochemical properties of high entropy alloys—A comparison with type-304 stainless steel. *Corros. Sci.* **2005**, *47*, 2257–2279. [[CrossRef](#)]
21. Qiu, X. Microstructure, hardness and corrosion resistance of Al₂CoCrCuFeNiTi_x high-entropy alloy coatings prepared by rapid solidification. *J. Alloys Compd.* **2018**, *735*, 359–364. [[CrossRef](#)]
22. Chou, Y.; Wang, Y.; Yeh, J.; Shih, H. Pitting corrosion of the high-entropy alloy Co_{1.5}CrFeNi_{1.5}Ti_{0.5}Mo_{0.1} in chloride-containing sulphate solutions. *Corros. Sci.* **2010**, *52*, 3481–3491. [[CrossRef](#)]
23. Gludovatz, B.; Hohenwarter, A.; Catoor, D.; Chang, E.H.; George, E.P.; Ritchie, R.O. A fracture-resistant high-entropy alloy for cryogenic applications. *Science* **2014**, *345*, 1153–1158. [[CrossRef](#)] [[PubMed](#)]
24. Tasan, C.C.; Deng, Y.; Pradeep, K.G.; Yao, M.J.; Springer, H.; Raabe, D. Composition dependence of phase stability, deformation mechanisms, and mechanical properties of the coCrFeMnNi high-entropy alloy system. *JOM* **2014**, *66*, 1993–2001. [[CrossRef](#)]
25. Lin, C.-M.; Juan, C.-C.; Chang, C.-H.; Tsai, C.-W.; Yeh, J.-W. Effect of Al addition on mechanical properties and microstructure of refractory Al_xHfNbTaTiZr alloys. *J. Alloys Compd.* **2015**, *624*, 100–107. [[CrossRef](#)]
26. Gali, A.; George, E. Tensile properties of high- and medium-entropy alloys. *Intermetallics* **2013**, *39*, 74–78. [[CrossRef](#)]
27. Chen, S.Y.; Wang, L.; Li, W.D.; Tong, Y.; Tseng, K.K.; Tsai, C.W.; Yeh, J.W.; Ren, Y.; Guo, W.; Poplawsky, J.D.; et al. Peierls barrier characteristic and anomalous strain hardening provoked by dynamic-strain-aging strengthening in a body-centered-cubic high-entropy alloy. *Mater. Res. Lett.* **2019**, *7*, 475–481. [[CrossRef](#)]
28. Gao, X.; Lu, Y.; Zhang, B.; Liang, N.; Wu, G.; Sha, G.; Liu, J.; Zhao, Y. Microstructural origins of high strength and high ductility in an AlCoCrFeNi_{2.1} eutectic high-entropy alloy. *Acta Mater.* **2017**, *141*, 59–66. [[CrossRef](#)]
29. Zhao, Y.; Yang, T.; Zhu, J.; Chen, D.; Yang, Y.; Hu, A.; Liu, C.; Kai, J.-J. Development of high-strength Co-free high-entropy alloys hardened by nanosized precipitates. *Scr. Mater.* **2018**, *148*, 51–55. [[CrossRef](#)]
30. Daoud, H.M.; Manzoni, A.; Wanderka, N.; Glatzel, U. High-temperature tensile strength of Al₁₀Co₂₅Cr₈Fe₁₅Ni₃₆Ti₆ compositionally complex alloy (high-entropy alloy). *JOM* **2015**, *67*, 2271–2277. [[CrossRef](#)]
31. Otto, F.; Dlouhý, A.; Somsen, C.; Bei, H.; Eggeler, G.; George, E.P. The influences of temperature and microstructure on the tensile properties of a CoCrFeMnNi high-entropy alloy. *Acta Mater.* **2013**, *61*, 5743–5755. [[CrossRef](#)]
32. Schuh, B.; Mendez-Martin, F.; Völker, B.; George, E.P.; Clemens, H.; Pippan, R.; Hohenwarter, A. Mechanical properties, microstructure and thermal stability of a nanocrystalline CoCrFeMnNi high-entropy alloy after severe plastic deformation. *Acta Mater.* **2015**, *96*, 258–268. [[CrossRef](#)]
33. Salishchev, G.; Tikhonovsky, M.; Shaysultanov, D.; Stepanov, N.; Kuznetsov, A.; Kolodiy, I.; Tortika, A.; Senkov, O. Effect of Mn and V on structure and mechanical properties of high-entropy alloys based on CoCrFeNi system. *J. Alloys Compd.* **2014**, *591*, 11–21. [[CrossRef](#)]
34. Zhang, A.; Han, J.; Su, B.; Li, P.; Meng, J. Microstructure, mechanical properties and tribological performance of CoCrFeNi high entropy alloy matrix self-lubricating composite. *Mater. Des.* **2017**, *114*, 253–263. [[CrossRef](#)]

35. Senkov, O.N.; Wilks, G.B.; Miracle, D.B.; Chuang, C.P.; Liaw, P.K. Refractory high-entropy alloys. *Intermetallics* **2010**, *18*, 1758–1765. [[CrossRef](#)]
36. Chen, S.; Li, W.; Meng, F.; Tong, Y.; Zhang, H.; Tseng, K.-K.; Yeh, J.-W.; Ren, Y.; Xu, F.; Wu, Z.; et al. On temperature and strain-rate dependence of flow serration in HfNbTaTiZr high-entropy alloy. *Scr. Mater.* **2021**, *200*, 113919. [[CrossRef](#)]
37. Senkov, O.N.; Scott, J.M.; Senkova, S.V.; Miracle, D.B.; Woodward, C.F. Microstructure and room temperature properties of a high-entropy TaNbHfZrTi alloy. *J. Alloys Compd.* **2011**, *509*, 6043–6048. [[CrossRef](#)]
38. Senkov, O.N.; Wilks, G.B.; Scott, J.M.; Miracle, D.B. Mechanical properties of Nb₂₅Mo₂₅Ta₂₅W₂₅ and V₂₀Nb₂₀Mo₂₀Ta₂₀W₂₀ refractory high entropy alloys. *Intermetallics* **2011**, *19*, 698–706. [[CrossRef](#)]
39. Juan, C.-C.; Tsai, M.-H.; Tsai, C.-W.; Lin, C.-M.; Wang, W.-R.; Yang, C.-C.; Chen, S.-K.; Lin, S.-J.; Yeh, J.-W. Enhanced mechanical properties of HfMoTaTiZr and HfMoNbTaTiZr refractory high-entropy alloys. *Intermetallics* **2015**, *62*, 76–83. [[CrossRef](#)]
40. Xian, X.; Zhong, Z.; Zhang, B.; Song, K.; Chen, C.; Wang, S.; Cheng, J.; Wu, Y. A high-entropy V₃₅Ti₃₅Fe₁₅Cr₁₀Zr₅ alloy with excellent high-temperature strength. *Mater. Des.* **2017**, *121*, 229–236. [[CrossRef](#)]
41. Tseng, K.-K.; Juan, C.-C.; Tso, S.; Chen, H.-C.; Tsai, C.-W.; Yeh, J.-W. Effects of Mo, Nb, Ta, Ti, and Zr on Mechanical Properties of Equiatomic Hf-Mo-Nb-Ta-Ti-Zr Alloys. *Entropy* **2018**, *21*, 15. [[CrossRef](#)]
42. Jung, Y.; Lee, K.; Hong, S.J.; Lee, J.K.; Han, J.; Kim, K.B.; Song, G. Investigation of phase-transformation path in TiZrHf (VNbTa) x refractory high-entropy alloys and its effect on mechanical property. *J. Alloys Compd.* **2021**, *886*, 161187. [[CrossRef](#)]
43. Tong, C.-J.; Chen, Y.-L.; Yeh, J.-W.; Lin, S.-J.; Chen, S.-K.; Shun, T.-T.; Tsau, C.-H.; Chang, S.-Y. Microstructure characterization of Al x CoCrCuFeNi high-entropy alloy system with multiprincipal elements. *Metall. Mater. Trans. A* **2005**, *36*, 881–893. [[CrossRef](#)]
44. Tsai, C.-W.; Chen, Y.-L.; Tsai, M.-H.; Yeh, J.-W.; Shun, T.-T.; Chen, S.-K. Deformation and annealing behaviors of high-entropy alloy Al_{0.5}CoCrCuFeNi. *J. Alloys Compd.* **2009**, *486*, 427–435. [[CrossRef](#)]
45. Li, B.; Wang, Y.; Ren, M.; Yang, C.; Fu, H. Effects of Mn, Ti and V on the microstructure and properties of AlCrFeCoNiCu high entropy alloy. *Mater. Sci. Eng. A* **2008**, *498*, 482–486. [[CrossRef](#)]
46. Tung, C.-C.; Yeh, J.-W.; Shun, T.-T.; Chen, S.-K.; Huang, Y.-S.; Chen, H.-C. On the elemental effect of AlCoCrCuFeNi high-entropy alloy system. *Mater. Lett.* **2007**, *61*, 1–5. [[CrossRef](#)]
47. Lee, C.; Chen, Y.Y.; Hsu, C.Y.; Yeh, J.W.; Shih, H.C. The effect of boron on the corrosion resistance of the high entropy alloys Al_{0.5}CoCrCuFeNiB x. *J. Electrochem. Soc.* **2007**, *154*, C424. [[CrossRef](#)]
48. Chen, S.-T.; Tang, W.Y.; Kuo, Y.F.; Chen, S.Y.; Tsau, C.H.; Shun, T.T.; Yeh, J.W. Microstructure and properties of age-hardenable AlxCrFe_{1.5}MnNi_{0.5} alloys. *Mater. Sci. Eng. A* **2010**, *527*, 5818–5825. [[CrossRef](#)]
49. Lee, C.; Chang, C.; Chen, Y.; Yeh, J.; Shih, H. Effect of the aluminium content of AlxCrFe_{1.5}MnNi_{0.5} high-entropy alloys on the corrosion behaviour in aqueous environments. *Corros. Sci.* **2008**, *50*, 2053–2060. [[CrossRef](#)]
50. Lee, C.; Chen, Y.; Hsu, C.; Yeh, J.; Shih, H. Enhancing pitting corrosion resistance of AlxCrFe_{1.5}MnNi_{0.5} high-entropy alloys by anodic treatment in sulfuric acid. *Thin Solid Films* **2008**, *517*, 1301–1305. [[CrossRef](#)]
51. Qin, G.; Chen, R.; Zheng, H.; Fang, H.; Wang, L.; Su, Y.; Fu, H. Strengthening FCC-CoCrFeMnNi high entropy alloys by Mo addition. *J. Mater. Sci. Technol.* **2019**, *35*, 578–583. [[CrossRef](#)]
52. Wang, M.; Ma, Z.; Xu, Z.; Cheng, X. Microstructures and mechanical properties of HfNbTaTiZrW and HfNbTaTiZrMoW refractory high-entropy alloys. *J. Alloys Compd.* **2019**, *803*, 778–785. [[CrossRef](#)]
53. Zhu, Y.; Guo, X.Y.; Liu, C.W.; Zhou, F.; Liu, B.Q. Effect of annealing temperature on the thermal stability of FeCrNiMnMo x Si_{0.5}B_{0.5} coatings. *Surf. Eng.* **2019**, *35*, 962–969. [[CrossRef](#)]
54. Shang, X.-L.; Wang, Z.J.; Wu, Q.F.; Wang, J.C.; Li, J.J.; Yu, J.K. Effect of Mo addition on corrosion behavior of high-entropy alloys CoCrFeNiMo x in aqueous environments. *Acta Metallurgica Sin.* **2019**, *32*, 41–51. [[CrossRef](#)]
55. Pardo, A.; Merino, M.; Coy, A.E.; Viejo, F.; Arrabal, R.; Matykina, E. Effect of Mo and Mn additions on the corrosion behaviour of AISI 304 and 316 stainless steels in H₂SO₄. *Corros. Sci.* **2008**, *50*, 780–794. [[CrossRef](#)]
56. Niu, Z.; Wang, Y.; Geng, C.; Xu, J.; Wang, Y. Microstructural evolution, mechanical and corrosion behaviors of as-annealed CoCrFeNiMo_x (x = 0, 0.2, 0.5, 0.8, 1) high entropy alloys. *J. Alloys Compd.* **2020**, *820*, 153273. [[CrossRef](#)]
57. Chou, Y.; Yeh, J.; Shih, H. The effect of molybdenum on the corrosion behaviour of the high-entropy alloys Co_{1.5}CrFeNi_{1.5}Ti_{0.5}Mo_x in aqueous environments. *Corros. Sci.* **2010**, *52*, 2571–2581. [[CrossRef](#)]
58. Batista, K.E.A.; Da Silva, J.L.F.; Piotrowski, M.J. Ab Initio Investigation of the Role of Atomic Radius in the Structural Formation of PtnTM_{55-n} (TM = Y, Zr, Nb, Mo and Tc) Nanoclusters. *J. Phys. Chem. C* **2018**, *122*, 7444–7454. [[CrossRef](#)]
59. Lubarda, V. On the effective lattice parameter of binary alloys. *Mech. Mater.* **2003**, *35*, 53–68. [[CrossRef](#)]
60. Sattar, T.; Lee, S.-H.; Jin, B.-S.; Kim, H.-S. Influence of Mo addition on the structural and electrochemical performance of Ni-rich cathode material for lithium-ion batteries. *Sci. Rep.* **2020**, *10*, 8562. [[CrossRef](#)] [[PubMed](#)]
61. Conejero, O.; Palacios, M.; Rivera, S. Premature corrosion failure of a 316L stainless steel plate due to the presence of sigma phase. *Eng. Fail. Anal.* **2009**, *16*, 699–704. [[CrossRef](#)]
62. Sieurin, H.; Sandström, R. Sigma phase precipitation in duplex stainless steel 2205. *Mater. Sci. Eng. A* **2007**, *444*, 271–276. [[CrossRef](#)]
63. Park, N.; Kim, I.; Na, Y.; Yeom, J. Hot forging of a nickel-base superalloy. *J. Mater. Process. Technol.* **2001**, *111*, 98–102. [[CrossRef](#)]
64. Hull, F. Effects of composition on embrittlement of austenitic stainless steels. *Weld. J.* **1973**, *52*, 104–113.
65. Carnot, A.; Frateur, I.; Zanna, S.; Tribollet, B.; Dubois-Brugger, I.; Marcus, P. Corrosion mechanisms of steel concrete moulds in contact with a demoulding agent studied by EIS and XPS. *Corros. Sci.* **2003**, *45*, 2513–2524. [[CrossRef](#)]

66. Li, X.-Y.; Akiyama, E.; Habazaki, H.; Kawashima, A.; Asami, K.; Hashimoto, K. The corrosion behavior of sputter-deposited amorphous Fe–Cr–Ni–Ta alloys in 12 M HCl. *Corros. Sci.* **1999**, *41*, 1849–1869. [[CrossRef](#)]
67. Zhang, L.; Xiang, Y.; Han, J.; Srolovitz, D.J. The effect of randomness on the strength of high-entropy alloys. *Acta Mater.* **2019**, *166*, 424–434. [[CrossRef](#)]
68. Vitek, V. Computer simulation of the screw dislocation motion in bcc metals under the effect of the external shear and uniaxial stresses. Proceedings of the Royal Society of London. *A. Math. Phys. Sci.* **1976**, *352*, 109–124.
69. Duesbery, M. On kinked screw dislocations in the b.c.c. lattice—II. Kink energies and double kinks. *Acta Met.* **1983**, *31*, 1759–1770. [[CrossRef](#)]
70. Hull, D.; Bacon, D.J. *Introduction to Dislocations*, 5th ed.; Elsevier: Amsterdam, The Netherlands, 2011; pp. 210–216.
71. Edahiro, T.; Kouzai, K.; Yasuda, H. Mechanical properties and hardening mechanism of Fe–Al–Ni single crystals containing NiAl precipitates. *Acta Mater.* **2013**, *61*, 1716–1725. [[CrossRef](#)]
72. Jumaev, E.; Hong, S.H.; Kim, J.T.; Park, H.J.; Kim, Y.S.; Mun, S.C.; Park, J.-Y.; Song, G.; Lee, J.K.; Min, B.H.; et al. Chemical evolution-induced strengthening on AlCoCrNi dual-phase high-entropy alloy with high specific strength. *J. Alloys Compd.* **2019**, *777*, 828–834. [[CrossRef](#)]
73. Jumaev, E.; Abbas, M.A.; Mun, S.C.; Song, G.; Hong, S.-J.; Kim, K.B. Nano-scale structural evolution of quaternary AlCrFeNi based high entropy alloys by the addition of specific minor elements and its effect on mechanical characteristics. *J. Alloys Compd.* **2021**, *868*, 159217. [[CrossRef](#)]
74. Miracle, D. Overview No. 104 The physical and mechanical properties of NiAl. *Acta Metallurgica Mater.* **1993**, *41*, 649–684. [[CrossRef](#)]
75. Cho, K.; Ikeda, K.; Yasuda, H.Y. Improvement of room and high temperature tensile properties of NiAl-strengthened ferritic heat-resistant steels through Mo addition. *Mater. Sci. Eng. A* **2018**, *728*, 239–250. [[CrossRef](#)]
76. Takasugi, T.; Kishino, J.; Hanada, S. Stress asymmetry of stoichiometric NiAl single crystals. *Acta Met. Mater.* **1993**, *41*, 1021–1031. [[CrossRef](#)]
77. Wang, Y.Q.; Han, J.; Wu, H.C.; Yang, B.; Wang, X.T. Effect of sigma phase precipitation on the mechanical and wear properties of Z3CN20.09M cast duplex stainless steel. *Nucl. Eng. Des.* **2013**, *259*, 1–7. [[CrossRef](#)]
78. Zhang, L.; Huo, X.; Wang, A.; Du, X.; Zhang, L.; Li, W.; Wu, B. A ductile high entropy alloy strengthened by nano sigma phase. *Intermetallics* **2020**, *122*, 106813. [[CrossRef](#)]
79. Sugimoto, K.; Sawada, Y. The role of molybdenum additions to austenitic stainless steels in the inhibition of pitting in acid chloride solutions. *Corros. Sci.* **1977**, *17*, 425–445. [[CrossRef](#)]
80. Ogawa, H.; Omata, H.; Itoh, I.; Okada, H. Auger Electron Spectroscopic and Electrochemical Analysis of the Effect of Alloying Elements on the Passivation Behavior of Stainless Steels. *Corrosion* **1978**, *34*, 52–60. [[CrossRef](#)]
81. Clayton, C.R.; Lu, Y.C. A bipolar model of the passivity of stainless steel: The role of mo addition. *J. Electrochem. Soc.* **1986**, *133*, 2465–2473. [[CrossRef](#)]
82. Sugimoto, K.; Sawada, Y. The Role of alloyed molybdenum in austenitic stainless steels in the inhibition of pitting in neutral halide solutions. *Corrosion* **1976**, *32*, 347–352. [[CrossRef](#)]
83. Hashimoto, K.; Asami, K.; Teramoto, K. An X-ray photo-electron spectroscopic study on the role of molybdenum in increasing the corrosion resistance of ferritic stainless steels in HCl. *Corros. Sci.* **1979**, *19*, 3–14. [[CrossRef](#)]
84. Lu, Y.C.; Clayton, C.R. Evidence for a Bipolar Mechanism of Passivity in Mo Bearing Stainless Steels. *J. Electrochem. Soc.* **1985**, *132*, 2517–2518. [[CrossRef](#)]
85. Kodama, T.; Ambrose, J.R. Effect of molybdate ion on the repassivation kinetics of iron in solutions containing chloride ions. *Corrosion* **1977**, *33*, 155–161. [[CrossRef](#)]
86. Pourbaix, M. Atlas of electrochemical equilibria in aqueous solution. *NACE* **1974**, *307–311*, 307–311.